

High-Entropy Alloys

Understanding Alkaline Hydrogen Oxidation Reaction on PdNiRuIrRh High-Entropy-Alloy by Machine Learning Potential

Yana Men⁺, Dean Wu⁺, Youcheng Hu⁺, Lei Li, Peng Li, Shuangfeng Jia, Jianbo Wang, Gongzhen Cheng, Shengli Chen,^{*} and Wei Luo^{*}

Abstract: High-entropy alloy (HEA) catalysts have been widely studied in electrocatalysis. However, identifying atomic structure of HEA with complex atomic arrangement is challenging, which seriously hinders the fundamental understanding of catalytic mechanism. Here, we report a HEA-PdNiRuIrRh catalyst with remarkable mass activity of 3.25 mA μg⁻¹ for alkaline hydrogen oxidation reaction (HOR), which is 8-fold enhancement compared to that of commercial Pt/C. Through machine learning potential-based Monte Carlo simulation, we reveal that the dominant Pd–Pd–Ni/Pd–Pd–Pd bonding environments and Ni/Ru oxophilic sites on HEA surface are beneficial to the optimized adsorption/desorption of *H and enhanced *OH adsorption, contributing to the excellent HOR activity and stability. This work provides significant insights into atomic structure and catalytic mechanism for HEA and offers novel prospects for developing advanced HOR electrocatalysts.

electrolyte even for the benchmark Pt/C,^[2] leading to much higher PGM catalysts loading at anode and unaffordable cost of fuel cell systems. Although significant progress has been made in the development of highly efficient low-Pt or Pt-free metal catalysts for alkaline HOR through the heterojunction or alloy engineering, such as Pt/Ni(OH)₂,^[3] PtRu/Mo₂C,^[4] IrPdRu/C^[5] and so on, the high-cost and inferior electrochemical stabilities in the HOR potential window still hinder their practical applications for AEMFC. Therefore, development of low-cost and highly efficient HOR catalysts with high stability under operating conditions is pivotal to promote the commercialization of AEMFC technology.

High-entropy-alloys (HEAs), containing five or more elements, have attracted considerable attentions owing to their multielement compositions and characteristic high-entropy mixing states.^[6] Compared to conventional mono-metals and binary alloys, HEAs possess unique atomic configurations and electronic structures, which are beneficial to the inherent synergistic effect, tunable catalytic activity and enhanced structural stability under operating conditions.^[7] Although initial efforts have been devoted to developing efficient HEA for electrocatalysis, the revelation of surface atomic distribution and coordination structures of HEA is suffering from the complex nearby coordination environment.^[8] Particularly, the investigation of electrocatalytic activity origin of HEA is limited by the conventional computational research paradigm, which is only applicable to system less than 100 atoms with specific surface atomic configuration for exploring adsorption thermodynamics of intermediates based on computational hydrogen electrode (CHE) model (e.g. density functional theory).^[9] However, due to the diverse surfaces caused by multielement distribution with larger atomic systems (at least more than 400 atoms), it is hard to implement the traditional density functional theory (DFT) calculation methods based on the CHE model proposed by Nørskov to directly investigate the thermodynamic adsorption process of elementary reaction and theoretically understand the electrocatalysis on the HEA surfaces,^[10] which severely hinders the fundamental understanding of catalytic mechanism. In this regard, Rossmeisl and co-workers have made very representative contributions in the structure determination, component optimization, and performance prediction for HEA, and developed corresponding machine learning methods and tools.^[11] More importantly, the use of HEA for HOR has been rarely reported, and the enhancement mechanism of stability of HEA under HOR conditions is still elusive so

Introduction

Compared to the advanced proton exchange membrane fuel cell (PEMFC), anion exchange membrane fuel cell (AEMFC) is considered to be more cost-effective due to the development of highly efficient platinum-group metal (PGM) free catalysts for the cathodic oxygen reduction reaction (ORR).^[1] Nevertheless, the anodic hydrogen oxidation reaction (HOR) severely suffers from the sluggish kinetics at high pH values, which is often approximately two to three orders of magnitude lower than that in acid

[*] Dr. Y. Men,⁺ D. Wu,⁺ Y. Hu,⁺ Dr. P. Li, Prof. Dr. G. Cheng, Prof. Dr. S. Chen, Prof. Dr. W. Luo
College of Chemistry and Molecular Sciences, Wuhan University
Wuhan, Hubei 430072 (P. R. China)
E-mail: slchen@whu.edu.cn
wluo@whu.edu.cn

Dr. L. Li
Core Facility of Wuhan University, Wuhan University
Wuhan, Hubei 430072 (P. R. China)

Dr. S. Jia, Prof. Dr. J. Wang
School of Physics and Technology, Center for Electron Microscopy, MOE Key Laboratory of Artificial Micro- and Nano-structures, and Institute for Advanced Studies, Wuhan University
Wuhan, Hubei 430072 (P. R. China)

[†] These authors contributed equally to this work.

far. Consequently, fundamentally understanding the catalytic mechanism and designing the efficient and stable HEAs catalysts for HOR under alkaline conditions remain challenging.

Recently, machine learning potential, trained by the data sets from *ab initio* calculations, have emerged as a promising theory approach, which can perform simulations close to macro scale with both quantum accuracy and efficiency of empirical potential.^[12] As a result, the thermodynamic favorable surfaces of HEAs with complex atomic distribution can be accurately determined by machine learning-based Monte Carlo (ML–MC) simulations,^[9] for which the Nørskov's approach can be carried out on the well-solved surface atomic configurations of HEAs. Herein, HEA-PdNiRuIrRh nanoparticles (NPs) are fabricated through a facile wet chemical synthetic method. Nickel is selected in HEA because Ni-based materials are currently the most promising non-noble metal catalysts for alkaline HOR.^[13] Meanwhile, the Pd, Rh, Ru and Ir are chosen because these PGM catalysts have been considered to be the highly efficient electrocatalysts for alkaline HER/HOR except for Pt, for which the alloys formed by these metals with Ni often exhibit much higher catalytic activity than the monomeric metals.^[14] As expected, the HEA electrocatalyst achieves an ultrahigh mass activity of $3.25 \text{ mA } \mu\text{g}^{-1}$ towards HOR under alkaline electrolyte, which is 52, 26, 12, 7 and 8 times higher than those of pristine Pd, Ru, Rh, Ir and commercial Pt/C, respectively, outperforming most of state-of-the-art noble metal alloy-based catalysts. Through ML–MC simulation, a nanoparticle model of the obtained HEA is directly simulated to comprehensively uncover the atomic distribution and coordination environment, disclosing that the surface atomic distribution mainly consists of Pd and Ni atoms. Integrating the ML–MC simulation with the Nørskov's method (CHE model), we demonstrate that the dominant Pd–Pd–Ni and Pd–Pd–Pd bonding environments on the HEA surface play a prominent role in the optimal adsorption/desorption of adsorbed hydrogen ($^*\text{H}$) intermediate, which, together with the enhanced $^*\text{OH}$ adsorption strength, contributes to the outstanding alkaline HOR performance. Furthermore, combining cyclic voltammetry tests with machine learning potential simulation, we reveal that the stability enhancement of HEA is attributed to the surface coordinated Pd and Ni components.

Results and Discussion

The single-phase HEA-PdNiRuIrRh NPs were fabricated through a facile wet-chemistry method via a low-temperature fast reduction of equal molar amounts of five metal precursors using preheated triethylene glycol solution (TEG) as reducing agent and solvent. The atomic ratio of Pd/Ni/Ru/Ir/Rh is calculated to be 26.5:26.2:14.8:16.8:15.7 (Table S1), through inductively coupled plasma-atomic emission spectroscopy (ICP-AES) results. As shown in Figure 1a, the powder X-ray diffraction (PXRD) pattern reveals that the HEA presents characteristic crystal structure features with a face-centered cubic (fcc) structure, in

which the typical diffraction peaks located at about 40.4° , 47.1° and 68.7° can be assigned to (111), (200) and (220) planes of fcc phase, respectively.^[8] The unit cell of HEA with fcc crystal structure is schematically exhibited in the insert of Figure 1a, in which five elements are randomly distributed on all sites, including the eight vertices and six face centers of the fcc unit cell. Notably, the diffraction peaks positions of HEA NPs show positive shifts comparing with that of Pd while negative shifts comparing with that of Ni and Rh, suggesting the successful formation of single-phase HEA (Figure S1).

The low-magnification high-angle annular dark-field scanning transmission electron microscopy (HAADF-STEM) and TEM images show the dispersed HEA NPs with an average particle size of about 4.8 nm (Figure S2). Aberration-corrected atomic-resolution HAADF-STEM was further performed to reveal the local atomic arrangement and elemental distribution of HEA. As shown in the atomic-resolution ADF-STEM image of HEA (Figure 1b), the bright atomic columns are observed indexed along the [011] zone axis, which represent the metal atoms in the Z-contrast imaging mode. The average spacing of periodic lattice fringes is measured to be 2.2 \AA , which matches well with the (111) facet of crystal structure of HEA. The corresponding fast Fourier transformation (FFT) pattern of the HEA nanoparticle is shown in Figure 1c, wherein typical selected area electron diffraction (SAED) patterns of fcc structure with groups of (-11-1), (11-1) and (200) crystal planes at the zone axis of [011] are marked with small circles, in accordance with the simulated diffraction pattern of fcc crystal structure along the [011] direction (Figure 1d). The corresponding model in (111) plan along the [011] zone axis of fcc-phased HEA NPs is shown in Figure 1e. Moreover, a periodic array metal atomic columns along the [001] direction can be distinguished, with lattice spacing of 1.92 \AA assigned to the (200) plane (Figure 1f). The corresponding FFT pattern of the highlighted HEA nanoparticle (Figure 1g) matches well with the simulated SAED pattern of fcc structure with groups of (-220), (020) and (220) crystal planes indexed along the [001] zone axis (Figure 1h), further demonstrating the fcc structured HEA NPs. The corresponding atomic structure in (200) facet along the [001] direction of fcc-phased HEA nanoparticles is shown in Figure 1i. Furthermore, the linear intensity profile analysis was performed to reveal the metal atom arrangement. Two white dashed square regions are marked as aa' and bb' in Figure 1f. As shown in Figures 1j and 1k, the peaks of different intensities can be distinguished clearly in the fluctuations of the line intensity, which is consistent with the multielement composition characteristics of high entropy alloys according to the principle of the Z-contrast of ADF-STEM image.^[15] In addition, the HAADF-STEM-EDX elemental mappings reveal the well dispersion of five elements within the nanoparticles, indicating the formation of single-phase solid solution alloy (Figures 1l–q, Figures S3, and S4). The corresponding EDX spectra and element content analyses are shown in Figures S3g and S4g. Taken together, the idealized atomic model of HEA nanoparticle is shown in Figure 1r.

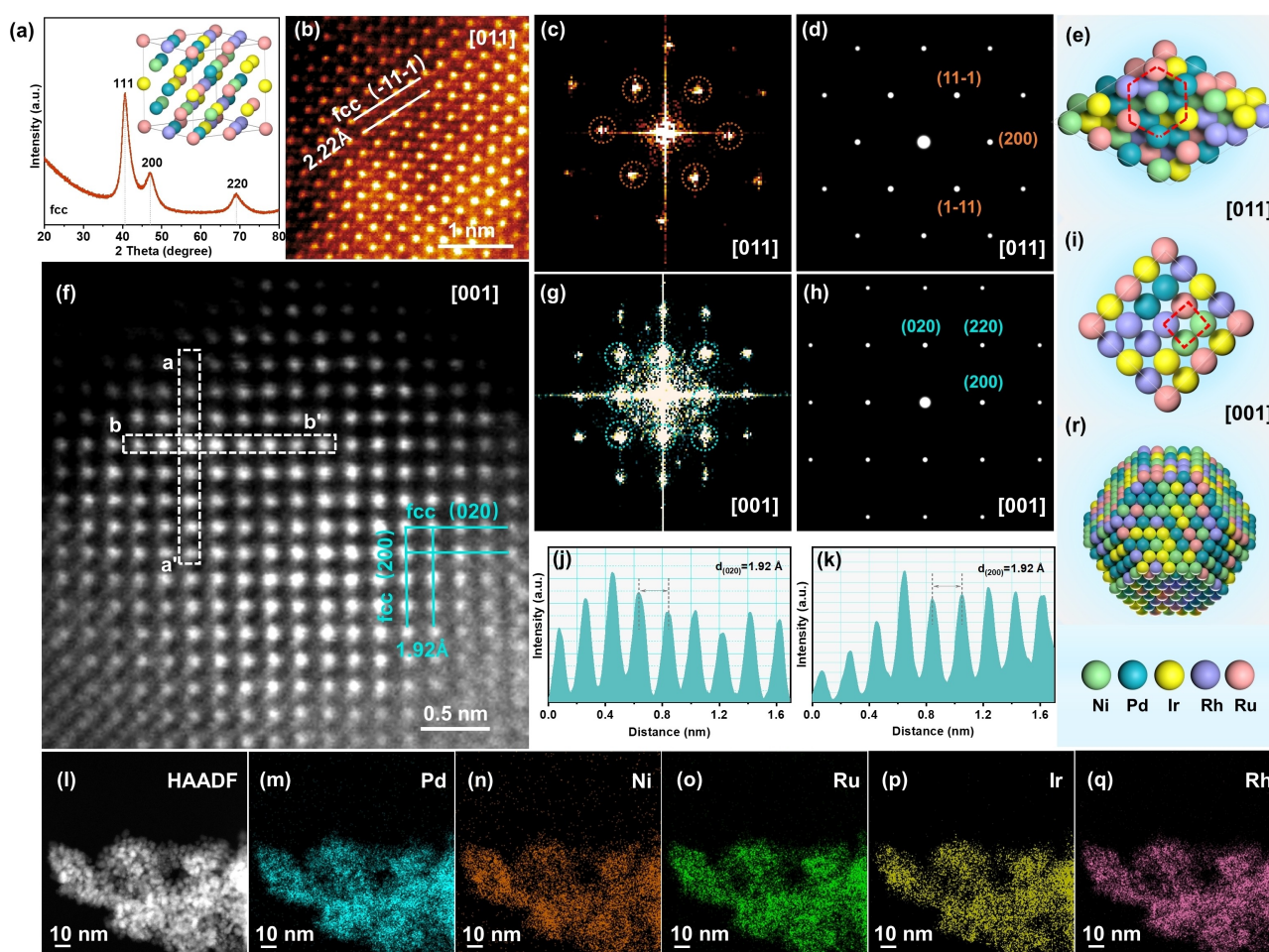


Figure 1. a) XRD pattern of HEA nanoparticles, the inset is the crystal structure (unit-cell) model of fcc HEA. b) Aberration-corrected atomic-resolution ADF-STEM image of HEA nanoparticles projected along the [011] zone axis and c) the corresponding fast Fourier transform (FFT) diffraction pattern. d) Simulated SAED pattern of fcc structure along the [011] zone axis. e) Simulated crystal structure in (111) plan along the [011] zone axis of fcc-phased HEA. f) Aberration-corrected atomic-resolution ADF-STEM image of HEA nanoparticles projected along the [001] zone axis and g) The corresponding fast Fourier transform (FFT) diffraction pattern. h) Simulated SAED pattern of fcc structure along the [001] zone axis. i) Simulated crystal structure in (200) plan along the [001] zone axis of fcc-phased HEA. j), k) Line intensity profiles taken from the white dashed square region (aa', bb'), respectively. l) HAADF-STEM image and the corresponding EDX elemental maps of Ni (m), Pd (n), Ir (o), Rh (p) and Ru (q). r) Simulated idealized atomic model of HEA nanoparticle.

X-ray photoelectron spectroscopy (XPS) measurements were carried out to reveal the surface elemental composition and valence states of HEA. As shown in Figure S5a, a pair of sharp peaks located at 335.4 and 340.7 eV can be observed in the high-resolution XPS spectra of Pd 3d, corresponding to Pd⁰ 3d_{5/2} and Pd⁰ 3d_{3/2}, respectively. The weak shoulder peaks at 336.6 and 342.1 eV belong to Pd²⁺ 3d_{5/2} and Pd²⁺ 3d_{3/2}, respectively.^[16] In the high-resolution XPS spectra of Ir 4f (Figure S5b), two sharp peaks at binding energies of 60.7 and 63.7 eV are assigned to Ir⁰ 4f_{7/2} and Ir⁰ 4f_{5/2}, respectively. In addition, the weak shoulder peaks located at 62.7 and 65.6 eV can be assigned to Ir⁴⁺ 4f_{7/2} and Ir⁴⁺ 4f_{5/2}, respectively.^[17] The XPS spectra of Ni 2p_{3/2} (Figure S5c) are divided into three peaks, which are corresponding to Ni⁰ 2p_{3/2}, Ni²⁺ 2p_{3/2} and shake-up satellites.^[18] As for the XPS spectra of Rh 3p_{3/2}, the main peak located at 495.1 eV is assigned to Rh⁰ 3p_{3/2}, and the small peak is attributed to the Rh²⁺ 3p_{3/2} (Figure S5d).^[19]

The XPS spectra of Ru 3p (Figure S5e) shows a group of sharp peaks at 461.3 and 483.3 eV, which are assigned to Ru⁰ 3p_{3/2} and Ru⁰ 3p_{1/2}, respectively.^[20] The trace metal oxidation states are possibly caused by surface oxidation when the catalyst is exposed in air.^[21] In addition, the surface element quantitative analysis was conducted through XPS. The comparison between the surface metal contents detected by XPS and the bulk contents determined by ICP-AES is shown in Figure S6 and Table S2. It can be clearly seen that the surface contents of Pd and Ni derived by XPS are greater than their bulk contents, indicating that these two elements are enriched on the surface of HEA catalysts.^[22]

The HOR performance of HEA catalysts were assessed by using the rotating disk electrode (RDE) voltammetry in H₂-saturated 0.1 M KOH electrolyte through a standard three-electrode setup. The electrocatalytic activity toward HOR of freshly synthesized Pd, Ni, Ru, Ir, Rh and bench-

mark Pt/C (20 wt% commercial Pt on Vulcan XC-72R carbon) were also investigated at the same condition for comparison. The HOR polarization curves of these samples were shown in Figure 2a, which were obtained by linear sweep voltammetry (LSV) measurement at a rotation speed of 1600 rpm. A rapidly increasing anode current can be observed unambiguously in the HOR polarization curve of HEA with the increase of potential. The HOR anode current density of HEA increases much faster at around 0 V vs reversible hydrogen electrode (RHE) than that of Pd, Ru, Ir, Rh, and the state-of-the-art commercial Pt/C, which is confirmed by the micro-polarization region (-5 to 5 mV) (Figure 2b). As shown in Figure 2c, the HOR polarization curves of HEA as a function of rotating speed from 625 rpm to 2500 rpm in H_2 -saturated 0.1 M KOH were also studied to obtain relevant kinetic parameters, wherein the plateau

current density increases as the rotating speed increased, due to the promotion of mass transport. As shown in the inset of Figure 2c, the Koutecky–Levich plot was constructed at an overpotential of 0.2 V, showing a linear relationship between j^{-1} and $\omega^{-1/2}$ with a slope of 14.03 cm^2 per $\text{mA rpm}^{1/2}$, which is consistent with the theoretical value of 14.8 cm^2 per $\text{mA rpm}^{1/2}$, confirming the two-electron HOR process.^[23] In addition, the HOR polarization curves at different rotating speeds of the other samples and the corresponding Koutecky–Levich plots were shown in Figure S7, in which the slopes of these samples match well with the theoretical value. The kinetic current density (j^k) of the HEA catalyst was further measured by Koutecky–Levich equation. The j^k at 50 mV vs. RHE of the HEA catalyst for HOR reaches 22.67 mA cm^{-2} , which is about 31, 24, 8 and 7 times higher than those of Pd

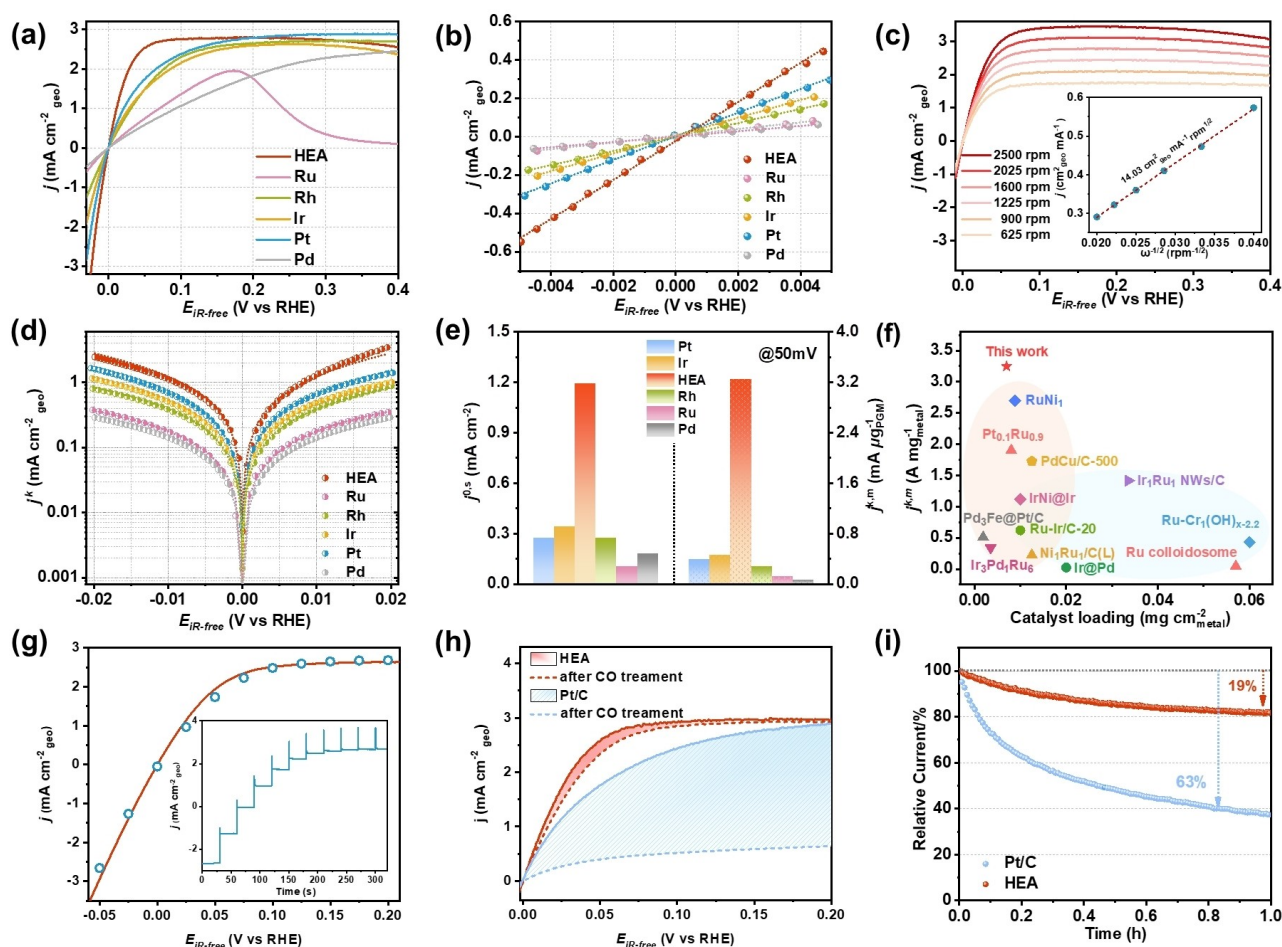


Figure 2. Electrocatalytic alkaline HOR performances. a) HOR polarization curves of HEA, Pd, Ru, Ir, Rh and commercial Pt/C in H_2 -saturated 0.1 M KOH at a rotation rate of 1600 rpm. b) Linear fitting curves of samples in the micro-polarization region. c) HOR polarization curves for HEA at various rotation speeds, respectively. Inset curve is the corresponding Koutecky–Levich plot at an overpotential of 0.2 V. d) Tafel plots of HEA, Pd, Ru, Ir, Rh and commercial Pt/C derived from (a) corresponding to the Butler–Volmer fitting. e) Comparison of the mass activities (j^k_m) at 50 mV and the ECSA-normalized exchange current densities (j^0_s) of HEA, Pd, Ru, Ir, Rh and commercial Pt/C. f) Comparison of j^k_m of HEA with those of recently reported advanced PGM-based catalysts, respectively. Details are listed in Table S3 and S4. g) The steady-state polarization curve (blue circles) converted from the inset curve, which is current density vs. time response of HEA to the potential program applied with the potential step of 25 mV, and the corresponding transient polarization curve obtained by CV. h) Comparison of the HOR polarization curves of Pt/C and HEA in H_2 -saturated 0.1 M KOH before and after the chronoamperometry test. i) Chronoamperometry curves of Pt/C and HEA in H_2 (100 ppm CO)-saturated 0.1 M KOH measured at 0.05 V vs RHE.

(0.72 mA cm⁻²), Ru (0.94 mA cm⁻²), Ir (2.67 mA cm⁻²), Rh (3.08 mA cm⁻²), respectively, and even represents 6-fold enhancement compared with the commercial Pt/C (3.93 mA cm⁻²). Figure 2d shows the Tafel plots of all samples derived from the Butler–Volmer fitting, from which the exchange current density (j^0) can be obtained. The electrochemical surface area (ECSA) of catalysts were evaluated by using copper underpotential deposition (Cu_{upd}) stripping voltammetry and cyclic voltammetry to determine the exchange current density (denoted as $j^{0,s}$).^[24] As shown in Figure 2e, after being normalized by the ECSA (Figures S8 and S9), the value of $j^{0,s}$ of HEA is measured to be 1.19 mA cm⁻², which is about 7, 11, 4 and 4 times higher than those of Pd (0.179 mA cm⁻²), Ru (0.105 mA cm⁻²), Ir (0.344 mA cm⁻²), Rh (0.273 mA cm⁻²), respectively, and represents about 4-fold enhancement compared with the commercial Pt/C (0.274 mA cm⁻²). It is worth noting that the $j^{0,s}$ of HEA is higher than most of the reported state-of-the-art PGM HOR catalysts as shown in Table S3. In addition, the values of $j^{0,s}$ of these samples are consistent well with the fitting data derived from the simplified Butler–Volmer equation in the micro-polarization region (Table S4), indicating the rationality of data fitting. Furthermore, the alkaline HOR activity of binary (PdNi), ternary (PdNiRu), quaternary (PdNiIrRu) alloys and other HEA with different component ratios (HEA-1, HEA-2) were also investigated. As shown in Figures S10–S12 and Table S5, the HEA still possesses the best catalytic performance among all the samples. The mass activity denoted as $j^{k,m}$ of HEA at 50 mV was also estimated by normalizing the metal loading on the electrode measured based on the results of ICP-AES. As shown in Figure 2e and Table S4, the value of $j^{k,m}$ of HEA is calculated to be 3.25 mA μg⁻¹, which is about 52, 26, 12, 7 and 8 times higher than those of Pd (0.063 mA μg⁻¹), Ru (0.124 mA μg⁻¹), Rh (0.277 mA μg⁻¹), Ir (0.455 mA μg⁻¹), and commercial Pt/C (0.386 mA μg⁻¹), respectively. Most notably, the $j^{k,m}$ of HEA is superior to most of the reported state-of-the-art PGM HOR catalysts (Figure 2f and Table S3), indicating the outstanding mass activity of HEA for alkaline HOR. In order to avoid the interference of non-Faradaic current, the HOR current density dependence on steady state was determined experimentally. As shown in the inset of Figure 2g, the HOR current density on time response of the HEA catalyst was measured by applying potential program. The steady state polarization curve (blue circles) was collected from the current density vs. time response curve, which is coincide well with the transient state polarization curve (red solid line), indicating no oxidation current of metals species under this potential condition (Figure 2g).^[25] The steady state curve (circle) at the micro-polarization regions was also obtained by the similar approach (Figure S13), which matches well with the transient state curve (red solid line), further suggesting the rationality of exchange current density calculation. Given that the fuel cell system is inevitably poisoned by CO impurity gas in hydrogen,^[26] the CO tolerances of the obtained catalysts were further evaluated. The chronoamperometry measurement was performed in H₂ gas mixed with 100 ppm CO saturated 0.1 M KOH to evaluate the CO

tolerance of HEA. The commercial Pt/C was also estimated under the same condition for comparison. As shown in Figure 2h, i, the rapidly decreased current density (decreased by 63 %) on Pt/C electrode during the chronoamperometry test can be observed. As a result, the HOR polarization curve suffers a seriously decline with the j^0 decreased by 74.8 %, comparing with the initial state (Figure S14). In contrast, the HOR polarization curve of HEA shows slightly decline with j^0 decreased by 15.5 %, comparing with the initial state (Figure S14), suggesting the high durability and excellent tolerance to CO poisoning of HEA.

Precisely revealing atomic structure and local coordination environment of HEA is crucial for further exploring the origin of high activity and stability. However, it is challenging for traditional ab initio calculations due to the diverse surfaces of HEA with larger atomic systems. To obtain the thermodynamically favorable configuration of HEA with atomic distribution, machine learning-based Monte Carlo (ML–MC) simulation has been applied based on the constructed high-dimensional neutral network potential of Pd_mNi_nRu_xIr_yRh_z system (see Section S1, Figures S15–S18).^[27] Figures S19 and S20 show the accuracy and reliability evaluations of the obtained machine learning potential for HEA–PdNiRuIrRh system. Then, the origin of enhancement of activity and stability for HEA electrocatalyst were investigated through combining the density functional theory (DFT) calculations based on computational hydrogen electrode (CHE) model.^[10] As shown in Figure 3a, the associated structure of HEA is modeled by the truncated octahedron nanoparticle with a radius of around 3 nm and optimized by the ML–MC simulation to obtain the thermodynamic favorable structures. For the optimized nanoparticle (right panel of Figure 3a), the layer-dependent fraction of elements distribution in the surface, sub-surface and third layers were performed. Figure 3b shows clearly that most of Pd atoms are distributed in the surface layer due to its relatively low surface energy,^[28] while Ni and Ir atoms are the main components in the sub-surface and third layer, respectively. It is in line with previous reports that the enrichment of one or more element(s) in the surface layers of HEA often occurs.^[29] More importantly, it is noted that such elements distribution features are not dependent on the HEA nanoparticle sizes (Figures S21 and S22), which confirms the rationality and reliability of the selected 3 nm particle model. Furthermore, the atomic coordination environment for each element in the nanoparticle is analyzed. Figure 3c and Figure S23 show that in the nanoparticle model of HEA, each element coordinates with various elements, which indicates the relatively uniform distribution of each composition in HEA, thereby creating diverse local coordination environments, which is responsible for the enhanced HOR activity. It worth noting that the wet synthesis approach in this work might lead to a more equilibrium distribution of elements near the surface of the nanoparticles, compared to the bulk. Meanwhile, the ML–MC simulations achieve quasi-equilibrium distribution of elements of HEA, thereby leading to effectively simulated surface elements distribution and coordination environment, which match well with the

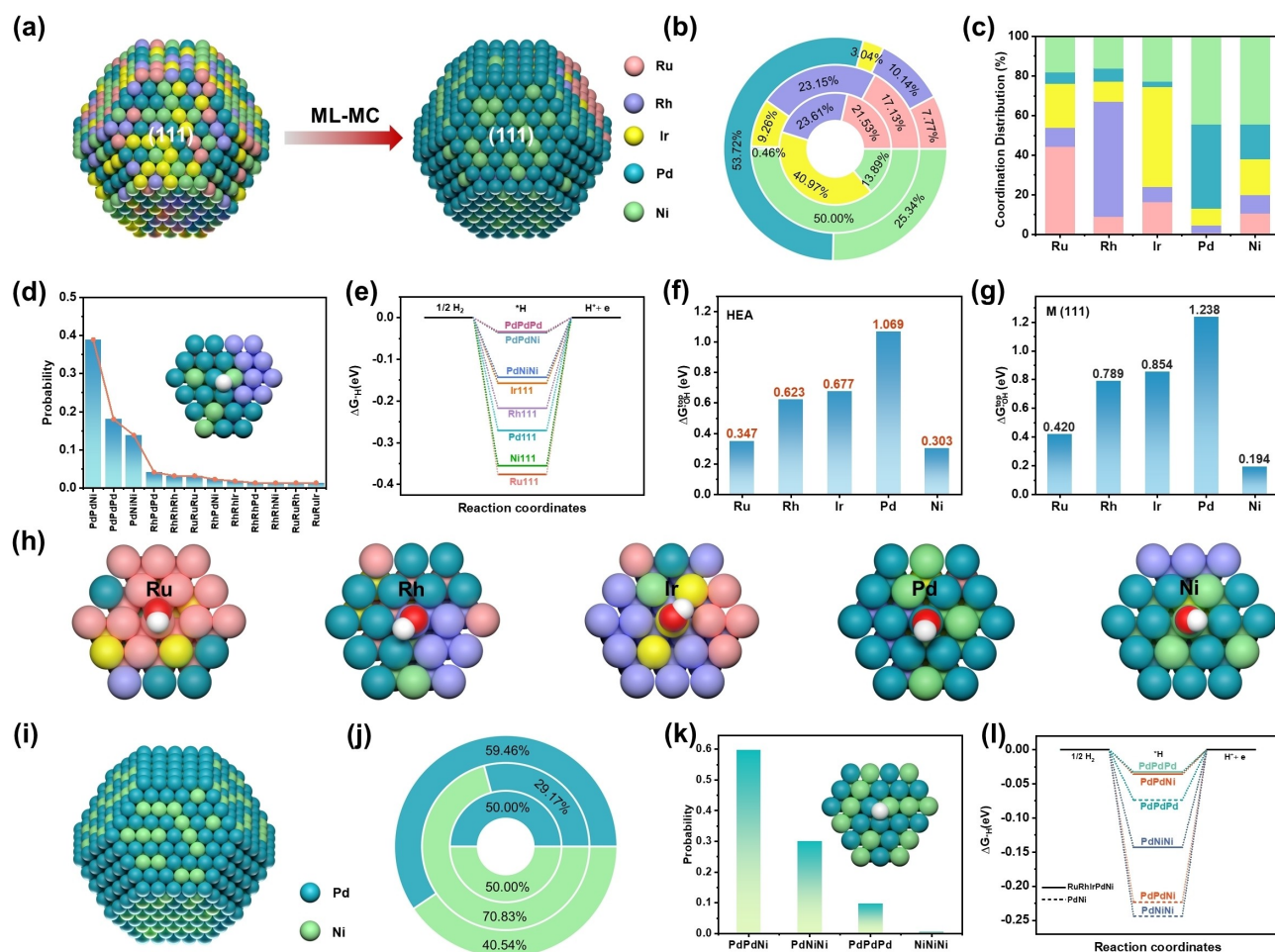


Figure 3. a) Structure optimization for the nanoparticle model of HEA through the ML–MC simulation. b) Layer-dependent fraction of elements distribution analysis for the surface, subsurface and the third atomic layer in (111) facet of HEA nanoparticle. c) Analyses of the atomic coordination environments for the HEA nanoparticle model. d) Identification of the types of hollow-fcc sites and the statistic of the proportion of each type of hollow-fcc site for the (111) facet of HEA nanoparticle. The inset is adsorption structure of *H on the hollow-fcc site. e) Adsorption free energies of *H on the hollow-fcc sites of HEA and pure metal (111) facet. f) Adsorption free energies of *OH on the top sites of various metal centers on HEA nanoparticle surface. g) Adsorption free energies of *OH on the top sites of metal centers for the (111) surfaces of pure metals. h) Adsorption structures of *OH on the top sites of HEA. i) The optimized nanoparticle model of PdNi alloy. j) Layer-dependent fraction of elements distribution analysis for the surface, subsurface and the third atomic layer in (111) facet of PdNi nanoparticle. k) Identification of the types of hollow-fcc sites and the statistic of the proportion of each type of hollow-fcc site for the (111) facet of PdNi nanoparticle. l) Comparison of the adsorption free energies of *H on the Pd–Pd–Ni, Pd–Ni–Ni and Pd–Pd–Pd hollow-fcc sites for HEA and PdNi.

experimental results. Nevertheless, the development of more efficient and accurate simulation strategies, such as combining MC simulation and enhanced sampling methods,^[30] will be highly necessary to obtain the true equilibrium configurations of complex HEA catalysts, which should be explored in the future.

Based on the above thermodynamically favorable structure of HEA, the origin of the high alkaline HOR activity is explored combining with the ab initio calculations (see Section S2). Due to the limitation of size in DFT method, the appropriate cut surface model is constructed through cutting the (111) facet of HEA nanoparticle (Figure S24), to calculate the adsorption energetics of key reaction intermediates (*H and *OH) in alkaline HOR process. First, for the *H intermediate, it is widely believed that the hydrogen atom is generally adsorbed on the hollow-fcc site of (111)

surface,^[31] which consists of three atoms. In this regard, the aforementioned coordination environment analyses show that the relatively uniform element distribution will create multifarious adsorption sites. Therefore, the types of hollow-fcc sites were first identified, and the proportion of each type of hollow-fcc site was counted. As shown in Figure 3d, the hollow-fcc sites consisting of Pd and Ni elements (Pd–Pd–Ni, Pd–Pd–Pd and Pd–Ni–Ni) on the HEA nanoparticle surface are predominant, due to the predominant Pd and Ni atoms on the surface. The adsorption structure of *H on the hollow-fcc site of HEA nanoparticle is shown in the inset of Figure 3d. The hydrogen adsorption free energies (ΔG_{H^+}) on these three dominant hollow-fcc sites of HEA are much more thermo-neutral compared to those on the (111) surfaces of various pure metals (Figure 3e), which is beneficial to the enhanced HOR kinetics. Moreover, it

can be seen that the dominant Pd–Pd–Pd and Pd–Pd–Ni hollow-fcc sites on the HEA surface also possess the most optimal ΔG_{H^+} among various hollow-fcc sites (Figure S25), further confirming the vital role of the Pd–Pd–Ni and Pd–Pd–Pd bonding environments in accelerating the alkaline HOR process.

It was reported that a moderately enhanced adsorption strength of *OH is beneficial to reducing the energy barrier of Volmer step according to the Brønsted-Evans-Polanyi (BEP) relation and thereby facilitating the alkaline HOR process.^[32] Therefore, the adsorption free energy of *OH ($\Delta G_{^*OH}$) on the HEA nanoparticle surface and the (111) surfaces of various pure metals were calculated. The top sites of surface metal atoms are considered for *OH adsorption according to the adsorption configuration of *OH intermediate measured by Li and co-workers.^[33] It can be seen clearly that each component on HEA surface possesses a stronger adsorption strength for *OH intermediate, compared to the (111) surfaces of various pure metals, except the Ni component (Figures 3f and g). The adsorption structures of *OH on the top sites of HEA are shown in Figure 3h. Furthermore, it can be seen unambiguously that for both the HEA and pure metals, the Ru and Ni possess the most oxophilic sites, which implies that these two components in the HEA are very likely the active sites of *OH intermediate. Although the adsorption strength of *OH on the pure Ni(111) surface is stronger than that on the Ni sites of HEA, the experimental alkaline HOR activity is still much poorer compared to HEA, which can be attributed to the unfavorable adsorption of *H intermediate. These results indicate that both optimized adsorption strengths of *H and *OH intermediates are essential for alkaline HOR.

On the other hand, the nanoparticle model of PdNi binary alloy has also been simulated through the ML–MC method to understand the roles of Ru, Rh and Ir elements in boosting alkaline HOR activity, which are predominant in the sub-surface. The optimized atomic structure of PdNi alloy and the layer-dependent fraction of elements distribution analysis are shown in Figures 3i and j. Figure 3k shows that on the PdNi nanoparticle surface, the Pd–Pd–Ni, Pd–Ni–Ni and Pd–Pd–Pd hollow-fcc sites are also predominant, which is in line with the HEA nanoparticle. Nevertheless, as shown in Figure 3l, the adsorption strength of *H intermediate on these three kinds of hollow-fcc sites for PdNi alloy are more deviant from thermo-neutral, compared to those on HEA. This result indicates that the Ru, Rh and Ir components in HEA can regulate the electronic structures of Pd and Ni components, thereby results in the optimized hydrogen binding energy on HEA, and significantly promoted alkaline HOR performance.

The favorable stability of HEA under operating conditions has usually been praised due to the unique high-entropy mixing states.^[34] However, the stability enhancement mechanism of HEA for alkaline HOR has not been investigated. Based on the deep machine learning potential simulation, we have first explored the origin of superior stability of HEA toward HOR. The electrochemical stability of HEA nanoparticle is evaluated by the

dissolving capacity of surface metal atoms from the stable (111) facet to form a vacancy (Figure 4a). In order to further compare the electrochemical stability of HEA with that of pure metal, the relative dissolving capacity between them have been obtained by calculating the difference of reaction energy (ΔE_r) of the dissolving processes on HEA nanoparticle (111) facet and pure metal (111) surface (see section S3 for details). A more positive ΔE_r value represents the higher electrochemical stability of HEA nanoparticle than pure metal. Figure 4b shows that the Ni component on the HEA nanoparticle surface is much more stable comparing with the pure Ni (111) surface, providing a great contribution to the excellent electrochemical stability of HEA. For the surface enriched Pd component, it can be seen that almost all Pd sites possess a positive ΔE_r value, indicating that the Pd atom possesses a significant enhancement of stability in HEA compared to pure Pd metal. Moreover, as for the Ru, Rh and Ir components with less surface distribution in HEA, they display balance on stability compared with the pure metal, which implies that the excellent electrochemical stability of HEA is mainly derived from the coordination of surface enriched Pd and Ni atoms. To further understand the enhancement mechanism of HEA, the heat maps of ΔE_r for all metal sites on the (111) facets of HEA nanoparticle were analyzed (Figure 4c). It clearly shows that the Pd sites adjacent to the Ru, Rh and Ir components usually possess more negative ΔE_r values (marked by the red dashed box); while for the remaining surface regions without the distributions of Ru, Rh and Ir, all the Pd and Ni sites display more positive ΔE_r values, demonstrating surface coordination of Pd and Ni components contributes to the electrochemical stability of HEA.

To verify the above simulation results, the accelerated durability tests (ADT) were conducted to evaluate the stability of catalysts through performing 1000 cycles of cyclic voltammetric (CV) measurement in 0.1 M Ar-saturated KOH solution. As shown in Figures 4d–g, the HOR polarization curve of HEA are almost coincides with the initial state after 1000 CV cycles. Moreover, the XRD pattern of HEA after stability test reveal the stable crystalline phase (Figure S26), further indicating the good stability of HEA toward alkaline HOR. In contrast, the polarization curves of the reference samples decreased rapidly after 1000 CV cycles (Figure 4e–g and Figure S27). Moreover, detailed kinetic analyses were performed. As shown in Figure 4h, the value of j^0 on HEA electrode has only decreased by 4.8 % of its original value, indicating the superior stability of HEA, which is consistent with the ML–MC simulation. However, the j^0 decreased by 20.6 %, 31.5 %, 31.5 %, and 35.3 % for Pd, Ru, Rh and Ir, respectively, indicating the poor electrochemical stability.

Conclusion

In summary, a HEA–NiPdRuIrRh electrocatalyst with superior stability for alkaline HOR has been developed by using facile wet-chemical strategy. Machine learning potential-based Monte Carlo (ML–MC) simulations unveil the

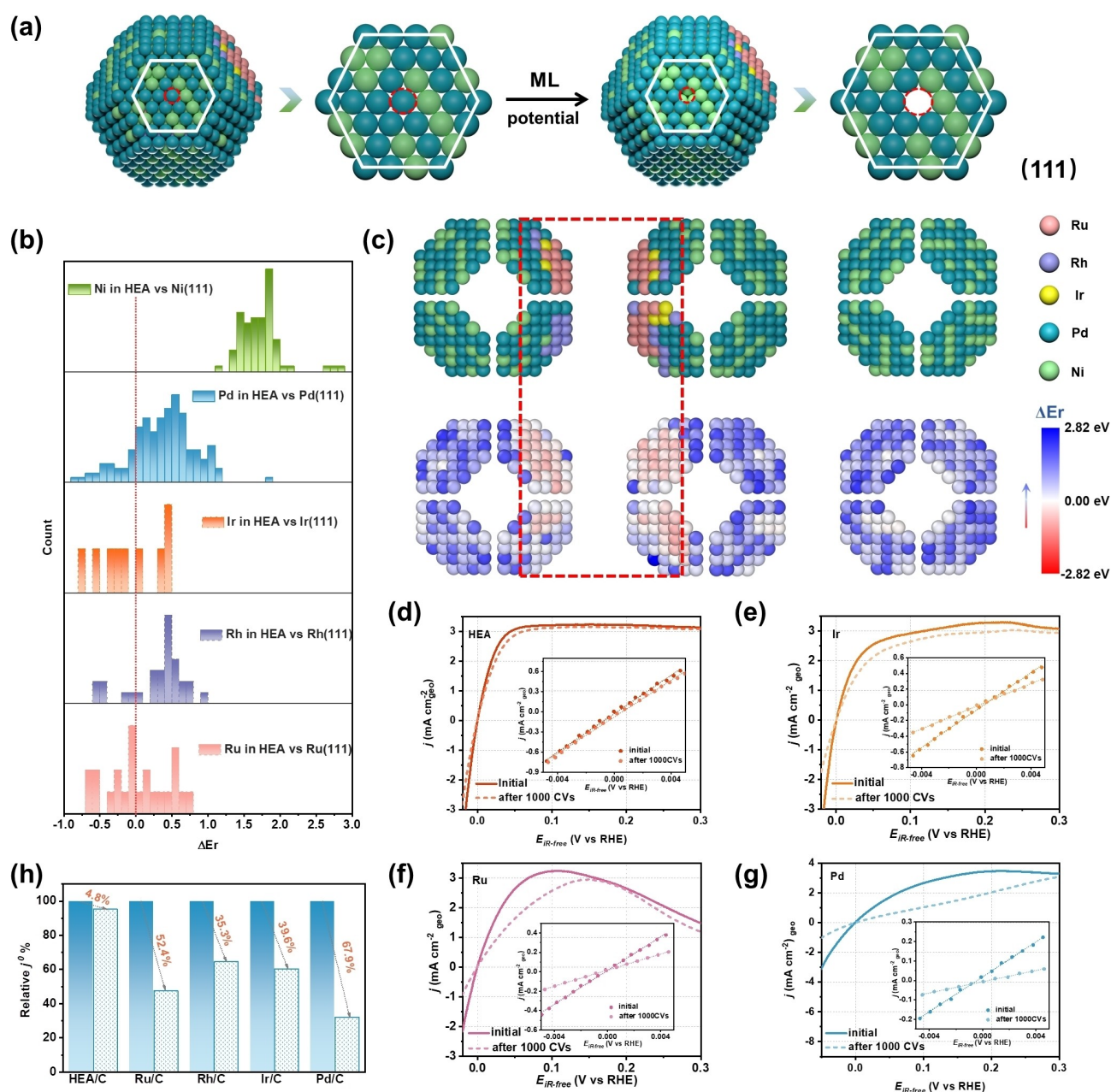


Figure 4. a) The schematic of the dissolving process of surface metal atom in HEA nanoparticle to evaluate the stability. The energies of various nanoparticle systems are obtained based on the trained machine learning potential. b) Statistic of the ΔE_r value for each component on the HEA nanoparticle (111) facet to represent the stability. c) The ΔE_r heat map of the HEA nanoparticle (111) facets. The upper panels are the atomic structure, and the lower panels are the corresponding heat map. d)–g) Accelerated durability tests for (d) HEA, (e) pure Ir, (f) pure Ru and (g) Pd. h) Comparison of j^0 before and after 1000 CVs.

atomic distribution of element components, surface atomic structures and local coordination environments of HEA, identifying the predominant surface atomic distribution of Pd and Ni atoms. By integrating the ML–MC simulation with the ab initio calculations based on the CHE model, we reveal that the dominant Pd–Pd–Ni/Pd–Pd–Pd bonding environments in the obtained HEA–NiPdRuIrRh enable optimal adsorption/desorption of $\ast\text{H}$ intermediate, which together with the enhanced $\ast\text{OH}$ adsorption strength derived from Ni and Ru oxophilic sites, contributes to the

remarkable alkaline HOR performance, with a mass activity of $3.25 \text{ mA } \mu\text{g}^{-1}$, which is 52, 26, 12, 7 and 8 times higher than those of the Pd, Ru, Rh, Ir and commercial Pt/C, respectively. Moreover, the HEA shows excellent CO tolerance than that of commercial Pt/C. Combining CV tests with machine learning potential simulation, we demonstrate that the surface coordination of Pd and Ni components play a critical role in enhancing stability of HEA. This study sheds light on atomic distribution and local atomic structures of HEA for fundamentally understanding the catalytic

mechanism and paves a new avenue for developing advanced HOR electrocatalysts.

Acknowledgements

The authors gratefully acknowledge the financial support from the National Key Research and Development Program of China (2021YFB4001200), National Natural Science Foundation of China (22272121, 21972107), Fundamental Research Funds for the Central Universities (2042022kf1179), Natural Science Foundation of Hubei Province (2020CFA095), and China Postdoctoral Science Foundation (2022M722453). We also thank the Supercomputing Center of Wuhan University and Core Facility of Wuhan University.

Conflict of Interest

The authors declare no conflict of interest.

Data Availability Statement

The data that support the findings of this study are available in the Supporting Information of this article.

Keywords: Atomic Structure • High-Entropy Alloys • Hydrogen Oxidation Reaction • Machine Learning • Monte Carlo Simulation

- [1] a) H. A. Gasteiger, N. M. Marković, *Science* **2009**, *324*, 48–49; b) B. P. Setzler, Z. Zhuang, J. A. Wittkopf, Y. Yan, *Nat. Nanotechnol.* **2016**, *11*, 1020–1025; c) Z. F. Pan, L. An, T. S. Zhao, Z. K. Tang, *Prog. Energy Combust. Sci.* **2018**, *66*, 141–175; d) X. Wu, N. Chen, H. A. Klok, Y. M. Lee, X. Hu, *Angew. Chem. Int. Ed.* **2022**, *61*, e202114892; e) Y. Gao, Y. Yang, R. Schimmenti, E. Murray, H. Peng, Y. Wang, C. Ge, W. Jiang, G. Wang, F. J. DiSalvo, *Proc. Natl. Acad. Sci. USA* **2022**, *119*, e2119883119.
- [2] a) W. Sheng, H. A. Gasteiger, Y. Shao-Horn, *J. Electrochem. Soc.* **2010**, *157*, B1529–B1536; b) J. Durst, A. Siebel, C. Simon, F. Hasché, J. Herranz, H. A. Gasteiger, *Energy Environ. Sci.* **2014**, *7*, 2255–2260; c) L. Su, Y. Jin, D. Gong, X. Ge, W. Zhang, X. Fan, W. Luo, *Angew. Chem. Int. Ed.* **2023**, *62*, e202215585.
- [3] R. Subbaraman, D. Tripkovic, D. Strmcnik, K.-C. Chang, M. Uchiumura, A. P. Paulikas, V. Stamenkovic, N. M. Markovic, *Science* **2011**, *334*, 1256–1260.
- [4] E. R. Hamo, R. K. Singh, J. C. Douglin, S. Chen, M. B. Hassine, E. Carbo-Argibay, S. Lu, H. Wang, P. J. Ferreira, B. A. Rosen, *ACS Catal.* **2021**, *11*, 932–947.
- [5] H. Wang, H. D. Abruña, *J. Am. Chem. Soc.* **2017**, *139*, 6807–6810.
- [6] a) Y. Yao, Z. Huang, P. Xie, S. D. Lacey, R. J. Jacob, H. Xie, F. Chen, A. Nie, T. Pu, M. Rehwoldt, *Science* **2018**, *359*, 1489–1494; b) Q. Ding, Y. Zhang, X. Chen, X. Fu, D. Chen, S. Chen, L. Gu, F. Wei, H. Bei, Y. Gao, *Nature* **2019**, *574*, 223–227; c) S. Gao, S. Hao, Z. Huang, Y. Yuan, S. Han, L. Lei, X. Zhang, R. Shahbazian-Yassar, J. Lu, *Nat. Commun.* **2020**, *11*, 2016; d) L. Tao, M. Sun, Y. Zhou, M. Luo, F. Lv, M. Li, Q. Zhang, L. Gu, B. Huang, S. Guo, *J. Am. Chem. Soc.* **2022**, *144*, 10582–10590; e) D. Wu, K. Kusada, T. Yamamoto, T. Toriyama, S. Matsumura, S. Kawaguchi, Y. Kubota, H. Kitagawa, *J. Am. Chem. Soc.* **2020**, *142*, 13833–13838.
- [7] P. Xie, Y. Yao, Z. Huang, Z. Liu, J. Zhang, T. Li, G. Wang, R. Shahbazian-Yassar, L. Hu, C. Wang, *Nat. Commun.* **2019**, *10*, 4011.
- [8] G. Feng, F. Ning, J. Song, H. Shang, K. Zhang, Z. Ding, P. Gao, W. Chu, D. Xia, *J. Am. Chem. Soc.* **2021**, *143*, 17117–17127.
- [9] L. Fan, Y. Ji, G. Wang, J. Chen, K. Chen, X. Liu, Z. Wen, *J. Am. Chem. Soc.* **2022**, *144*, 7224–7235.
- [10] J. K. Nørskov, J. Rossmeisl, A. Logadottir, L. Lindqvist, J. R. Kitchin, T. Bligaard, H. Jonsson, *J. Phys. Chem. B* **2004**, *108*, 17886–17892.
- [11] a) J. K. Pedersen, C. M. Clausen, O. A. Krysiak, B. Xiao, T. A. A. Batchelor, T. Löffler, V. A. Mints, L. Banko, M. Arenz, A. Savan, W. Schuhmann, A. Ludwig, J. Rossmeisl, *Angew. Chem. Int. Ed.* **2021**, *60*, 24144–24152; b) T. Löffler, A. Ludwig, J. Rossmeisl, W. Schuhmann, *Angew. Chem. Int. Ed.* **2021**, *60*, 26894–26903; c) J. K. Pedersen, T. A. A. Batchelor, D. Yan, L. E. J. Skjægstad, J. Rossmeisl, *Curr. Opin. Electrochem.* **2021**, *26*, 100651; d) T. A. A. Batchelor, J. K. Pedersen, S. H. Winther, I. E. Castelli, K. W. Jacobsen, J. Rossmeisl, *Joule* **2019**, *3*, 834–845.
- [12] a) J. Behler, *Angew. Chem. Int. Ed.* **2017**, *56*, 12828–12840; b) J. Behler, M. Parrinello, *Phys. Rev. Lett.* **2007**, *98*, 146401.
- [13] W. Ni, T. Wang, F. Héroguel, A. Krammer, S. Lee, L. Yao, A. Schüler, J. S. Luterbacher, Y. Yan, X. Hu, *Nat. Mater.* **2022**, *21*, 804–810.
- [14] a) Y. Liu, X. Li, Q. Zhang, W. Li, Y. Xie, H. Liu, L. Shang, Z. Liu, Z. Chen, L. Gu, Z. Tang, T. Zhang, S. Lu, *Angew. Chem. Int. Ed.* **2020**, *59*, 1718–1726; b) F. Chen, Y. Yao, A. Nie, S. Xu, J. Dai, E. Hitz, Y. Li, A. Lu, Z. Huang, T. Li, R. Shahbazian-Yassar, L. Hu, *Adv. Energy Mater.* **2018**, *8*, 1800466; c) X. Tian, P. Zhao, W. Sheng, *Adv. Mater.* **2019**, *31*, 1808066; d) Z.-C. Yao, T. Tang, Z. Jiang, L. Wang, J.-S. Hu, L.-J. Wan, *ACS Nano* **2022**, *16*, 5153–5183.
- [15] A. V. Crewe, J. Wall, J. Langmore, *Science* **1970**, *168*, 1338–1340.
- [16] a) L. Lu, X. Sun, J. Ma, D. Yang, H. Wu, B. Zhang, J. Zhang, B. Han, *Angew. Chem. Int. Ed.* **2018**, *57*, 14149–14153; b) M. Li, Z. Zhao, Z. Xia, M. Luo, Q. Zhang, Y. Qin, L. Tao, K. Yin, Y. Chao, L. Gu, *Angew. Chem. Int. Ed.* **2021**, *60*, 8243–8250.
- [17] L. Fu, Y. Li, N. Yao, F. Yang, G. Cheng, W. Luo, *ACS Catal.* **2020**, *10*, 7322–7327.
- [18] W. Ni, A. Krammer, C. S. Hsu, H. M. Chen, A. Schüler, X. Hu, *Angew. Chem. Int. Ed.* **2019**, *58*, 7445–7449.
- [19] R. Nyholm, N. Martensson, *J. Phys. C* **1980**, *13*, L279–L284.
- [20] Y. Xue, L. Shi, X. Liu, J. Fang, X. Wang, B. P. Setzler, W. Zhu, Y. Yan, Z. Zhuang, *Nat. Commun.* **2020**, *11*, 5651.
- [21] Y. Duan, Z.-Y. Yu, L. Yang, L.-R. Zheng, C.-T. Zhang, X.-T. Yang, F.-Y. Gao, X.-L. Zhang, X. Yu, R. Liu, H.-H. Ding, C. Gu, X.-S. Zheng, L. Shi, J. Jiang, J.-F. Zhu, M.-R. Gao, S.-H. Yu, *Nat. Commun.* **2020**, *11*, 4789.
- [22] a) Z. Niu, N. Becknell, Y. Yu, D. Kim, C. Chen, N. Kornienko, G. A. Somorjai, P. Yang, *Nat. Mater.* **2016**, *15*, 1188–1194; b) H. Liu, R. Jia, C. Qin, Q. Yang, Z. Tang, M. Li, Z. Ma, *Adv. Funct. Mater.* **2023**, *33*, 2210626; c) B.-A. Lu, L.-F. Shen, J. Liu, Q. Zhang, L.-Y. Wan, D. J. Morris, R.-X. Wang, Z.-Y. Zhou, G. Li, T. Sheng, L. Gu, P. Zhang, N. Tian, S.-G. Sun, *ACS Catal.* **2021**, *11*, 355–363; d) C. Zhang, X. Liang, R. Xu, C. Dai, B. Wu, G. Yu, B. Chen, X. Wang, N. Liu, *Adv. Funct. Mater.* **2021**, *31*, 2008298.
- [23] a) Z. Zhuang, S. A. Giles, J. Zheng, G. R. Jenness, S. Caratzoulas, D. G. Vlachos, Y. Yan, *Nat. Commun.* **2016**, *7*,

- 10141; b) J. Zheng, S. Zhou, S. Gu, B. Xu, Y. Yan, *J. Electrochem. Soc.* **2016**, *163*, F499–F506.
- [24] a) J. Ohyama, T. Sato, Y. Yamamoto, S. Arai, A. Satsuma, *J. Am. Chem. Soc.* **2013**, *135*, 8016–8021; b) L. Su, Y. Zhao, Y. Jin, Z. Liu, H. Cui, W. Luo, *Adv. Funct. Mater.* **2022**, *32*, 2113047.
- [25] Y. Zhao, F. Yang, W. Zhang, Q. Li, X. Wang, L. Su, X. Hu, Y. Wang, Z. Wang, L. Zhuang, S. Chen, W. Luo, *CCS Chem.* **2022**, *4*, 1732–1744.
- [26] Y. Men, X. Su, P. Li, Y. Tan, C. Ge, S. Jia, L. Li, J. Wang, G. Cheng, L. Zhuang, S. Chen, W. Luo, *J. Am. Chem. Soc.* **2022**, *144*, 12661–12672.
- [27] a) J. Han, L. Zhang, R. Car, W. E, arXiv:1707.01478v2 **2017**; b) L. Zhang, J. Han, H. Wang, R. Car, W. E, *Phys. Rev. Lett.* **2018**, *120*, 143001; c) L. Zhang, J. Han, H. Wang, W. Saidi, R. Car, *Adv. Neural Inform. Process. Syst.* **2018**, *31*, 4436–4446.
- [28] a) L. Vitos, A. V. Ruban, H. L. Skriver, J. Kollár, *Surf. Sci.* **1998**, *411*, 186–202; b) H. L. Skriver, N. M. Rosengaard, *Phys. Rev. B* **1992**, *46*, 7157–7168.
- [29] a) D. Chatain, P. Wynblatt, *Comput. Mater. Sci.* **2021**, *187*, 110101; b) C. Dahale, S. Goverapet Srinivasan, S. Mishra, S. Maiti, B. Rai, *Mol. Syst. Des. Eng.* **2022**, *7*, 878–888; c) N. L. N. Broge, M. Bondesgaard, F. Søndergaard-Pedersen, M. Roelsgaard, B. B. Iversen, *Angew. Chem. Int. Ed.* **2020**, *59*, 21920–21924.
- [30] a) Y. Q. Gao, *J. Chem. Phys.* **2008**, *128*, 064105; b) J. Kästner, *Wiley Interdiscip. Rev. Comput. Mol. Sci.* **2011**, *1*, 932–942.
- [31] T. Jacob, W. A. Goddard, *J. Phys. Chem. B* **2004**, *108*, 8311–8323.
- [32] a) D. Strmcnik, M. Uchimura, C. Wang, R. Subbaraman, N. Danilovic, D. van der Vliet, A. P. Paulikas, V. R. Stamenkovic, N. M. Markovic, *Nat. Chem.* **2013**, *5*, 300–306; b) I. T. McCrum, M. T. M. Koper, *Nat. Energy* **2020**, *5*, 891–899.
- [33] Y. H. Wang, X. T. Wang, H. Ze, X. G. Zhang, P. M. Radjenovic, Y. J. Zhang, J. C. Dong, Z. Q. Tian, J. F. Li, *Angew. Chem. Int. Ed.* **2021**, *60*, 5708–5711.
- [34] Y. Yao, Q. Dong, A. Brozena, J. Luo, J. Miao, M. Chi, C. Wang, I. G. Kevrekidis, Z. J. Ren, J. Greeley, G. Wang, A. Anapolsky, L. Hu, *Science* **2022**, *376*, eabn3103.

Manuscript received: December 6, 2022

Accepted manuscript online: May 2, 2023

Version of record online: May 19, 2023